# Cross-system biological image quality enhancement based on the generative adversarial network as a foundation for establishing a multi-institute microscopy cooperative network

Dominik Panek[a, b], Carina Rząca[a, b], Maksymilian Szczypior[b,c], Joanna Sorysz[d],
Krzysztof Misztal[e]*, Zbigniew Baster[b, †]*, Zenon Rajfur[b]*

[a] Doctoral School of Exact and Natural Sciences, Jagiellonian University, ul. Łojasiewicza 11, 30-348 Kraków, Poland
[b] Department of Molecular and Interfacial Biophysics, Faculty of Physics, Astronomy and Applied Computer Science, Jagiellonian University, ul. Łojasiewicza 11, 30-348 Kraków, Poland.
[c] Undergraduate program in Biophysics, Faculty of Physics, Astronomy and Applied Computer Science, Jagiellonian University, ul. Łojasiewicza 11, 30-348 Kraków, Poland.
[d] Undergraduate program in Biomedical Engineering, Faculty of Electrical Engineering, Automatics, Computer Science and Biomedical Engineering, AGH University of Science and Technology, Al. A. Mickiewicza 30, Building B-1, 30-059 Kraków, Poland.
[d] Division of Computational Mathematics, Faculty of Mathematics and Computer Science, Jagiellonian University, 6 Łojasiewicza St., Kraków, Poland
[†] Current address: Cell and Developmental Biology Center, National Heart Lung and Blood Institute, National Institutes of Health, Bethesda, MD 20824-0105, USA
*Author to whom correspondence should be addressed: krzysztof.misztal@uj.edu.pl, zbigniew.baster@nih.gov, zenon.rajfur@uj.edu.pl.

**Abstract**

High-quality fluorescence imaging of biological systems is limited by processes like photobleaching and phototoxicity, and also in many cases, by limited access to the latest generations of microscopes. Moreover, low temporal resolution can lead to a motion blur effect in living systems. Our work presents a deep learning (DL) generative-adversarial approach to the problem of obtaining high-quality (HQ) images based on their low-quality (LQ) equivalents. We propose a generative-adversarial network (GAN) for contrast transfer between two different separate microscopy systems: a confocal microscope (producing HQ images) and a wide-field fluorescence microscope (producing LQ images). Our model proves that such transfer is possible, allowing us to receive HQ-generated images characterized by low mean squared error (MSE) values, high structural similarity index (SSIM), and high peak signal-to-noise ratio (PSNR) values. For our best model in the case of comparing HQ-generated images and HQ-ground truth images, the median values of the metrics are $6 \cdot 10^{-4}$, 0.9413, and 31.87, for MSE, SSIM, and PSNR, respectively. In contrast, in the case of comparison between LQ and HQ ground truth median values of the metrics are equal to 0.0071, 0.8304, and 21.48 for MSE, SSIM, and PSNR respectively. Therefore, we observe a significant increase ranging from 14% to 49% for SSIM and PSNR respectively. These results, together with other single-system cross-modality studies, provide proof of concept for further implementation of a cross-system biological image quality enhancement.

## 1. Introduction

High-quality microscopy plays a crucial role in biological sciences [1,2]. The development of several groundbreaking techniques such as fluorescence confocal microscopy and later super-resolution techniques unlocked new possibilities in biological sciences like 3D optical sectioning and imaging nanometric size (5-20nm) structures [3–8]. Nowadays, these marvelous techniques have established their place well in the spectrum of research techniques, and it is hard to imagine doing research without them. Yet, even with years of further research and development, they still come with caveats like high cost of equipment or low imaging throughput, which drastically limit access to these essential techniques, especially in low-income regions [4]. On the other hand, techniques like basic wide-field fluorescence (WFF) microscopy are getting more and more accessible these days, especially if we consider that second-hand retired systems, which cost a fraction of their original price, often offer a good-quality basic WFF-based imaging potential [9,10]. These systems allow a fine-quality basic fluorescence imaging with reduced cost and time of a microscopy experiment, however without advantages that give more advanced techniques.

A generative-adversarial network (GAN) is one of the methods that can be used to bridge low-quality low-cost fast imaging with advantages given by confocal or super-resolution techniques. GANs are composed of two networks: a generator and a discriminator [11,12]. The crucial part of GAN training is the dynamic interplay between those two networks. GANs have been used in many different fields and are one of the most promising deep-learning methods [13–18]. This type of architecture has already been implemented for modalities, where images from the same imaging system were gathered in different resolutions to improve their quality after processing them through the network [19]. Moreover, different modifications of GANs were also proved to be efficient tools and showed promising results in other image-enhancement applications [13,14,19–21]. A great advantage of GAN is its easy way of implementing different modifications to the base architecture. For example, some alterations include Fourier Channel Attention blocks, which proved to be useful when STED and confocal images were compared [22]. However, it is worth noting that the more complex the implemented methods, the more computationally intensive the entire model will be, which can significantly increase the calculation time.

In our research, we created a database of matching pairs of images collected on two separate imaging systems: a wide-field fluorescence microscope, and a laser scanning confocal microscope. We developed a GAN model for deep-learning microscopy, where we recovered the spatial information from the LQ WFF microscopy images based on their HQ confocal equivalents (the ground truth data). In short, the generator aims to create the HQ image based on the LQ input. Next, the discriminator is primarily trained on the HQ ground truth images and later is fed with HQ-generated images to estimate the resemblance between the generated images and the ground truth ones [12]. In our GAN implementation, we used a U-NET architecture for the generator [23]. U-NET was first applied for the biological image segmentation methods but was also proved to be a robust architecture in our case. This type of network learns the features of the image in a very efficient way by employing down- and up-sampling blocks [24–29]. Furthermore, our U-NET architecture is modified with additional residues, which improve network performance even further. On the other hand, for the discriminator, we employed a simple convolutional neural network (CNN) architecture. The results received from our network, based on our cross-system database, together with other single-system cross-modality studies, provide proof of concept and a scientific basis for further implementation of cross-system biological image quality enhancement. In future, this may help to establish fundaments for forming a multi-institute microscopy cooperative network, where multiple microscopes, located even on different continents, may be virtually paired together to increase access to high-quality imaging methods.

## 2. Methods

In this research, we employed a GAN architecture. It consists of a discriminator and a generator, which work adversarially to obtain images, which would resemble images obtained using a high-quality modality. Original data was composed of 149 aligned images of mouse embryonic fibroblasts (procedure of data aligning was performed in ImageJ software [30–32], and is described in detail in the supplementary materials) obtained from laser scanning confocal (Zeiss LSM 710 set on Zeiss Axio Observer Z1 body, oil-immersion Plan-Apochromat 40x NA 1.4 objective, ZEN black version 8.10.484 software) and wide-field fluorescence microscopes (Zeiss Axio Observer Z1, oil-immersion EC Plan-Neofluar 40x NA 1.30 Ph3, ZEN blue version 2.3 software). They were later artificially augmented using data augmentation random flips, random rotations, and/or random translations algorithms (all actions were taken at the same time for LQ and HQ ground truth images). These procedures allowed us to increase the total number of images to around 600. Augmented data was split into training, testing, and validation subsets (80% - 19% - 1%, respectively). The training procedure is described below. The architecture of the network is shown in **Figure 1.** The Discriminator comprises a CNN with 10 convolutional blocks. It initiates with a convolutional layer, and its output is fed through subsequent convolutional blocks, where a series of essential operations unfold as follows:

$$x_k = LReLU[Conv2D(LReLU[Conv2D(LReLU[Conv2D(LReLU[Conv2D(x_{k-1})])])])], \quad \textbf{(1)}$$
$$k = 1, 2, \ldots, 10,$$

where $x_k$ is the output of the *x-th* convolutional block, $x_0$ is the input from the first convolutional layer, *LReLU* is a Leaky Rectified Linear Unit activation function with a slope *a= 0.1*, and *Conv2D* is a two-dimensional convolution operation. *LReLU* is defined as:

$$LReLU(x, a) = \max(0, x) - a \cdot \max(0, -x). \qquad \textbf{(2)}$$

After the 10th convolutional block, the average pooling layer is inserted to reduce dimensionality, implementing a 4x4 pool size. Subsequently, two fully connected layers (FC) are added and the network outputs the probability estimated by the sigmoid activation function. The generative model is based on a residual U-NET architecture, facilitating the acquisition of spatial information by the network. In this case, U-NET consists of 4 down-sampling and four up-sampling blocks, connected by skip layers. Each down-sampling block consists of 3 convolutional blocks, where the following operations are performed:

$$d_k = d_{k-1} + LReLU[Conv2D(LReLU[Conv(LReLU[Conv2D(d_{k-1})])])], \qquad \textbf{(3)}$$
$$k = 1, 2, 3, 4.$$

Following the addition operation, an average pooling layer is inserted with a 2x2 pool size. In this case, $d_0$ is the input image. Similarly, to the down-sampling part, the up-sampling blocks consist of three convolutional blocks with the following operations:

$$u_k = LReLU[Conv2D(LReLU[Conv2D(LReLU[Conv2D(Concat\{d_{5-k}, u_{k-1}\})])])], \qquad \textbf{(4)}$$
$$k = 1, 2, 3, 4$$

After the last block, a convolution layer, together with the *LReLU* activation function, is added. Here, $u_0$ denotes the output of the layer, which is placed at the bottom of the U-NET. The *Concat*

operation denotes the concatenation of the down-sampling, and up-sampling layers (so-called skipped connections), which allows to improve network performance.

The loss function employed in the discriminative model is a simple binary cross-entropy (BCE). Its primary objective is to determine whether the received images correspond to the HQ ground truth or are generated by the network, effectively acting as a binary classifier. BCE is defined as follows:

$$\mathcal{L}_{D|G}(X,Y) = BCE\big(D\big(G(X)\big) - D(Y), y\big) + BCE\big(D(Y) - D\big(G(X)\big), 1 - y\big), \tag{5}$$

where $X$ and $Y$ denote the LQ and HQ input images, respectively. $G(\cdot)$ is the generative model output, $D(\cdot)$ represents discriminator model prediction, and $y$ is the label set during the training (0 when the discriminator is trained). In the case of the generative model, the combined losses of MSE (mean squared error), SSIM (structural similarity index) [33], and BCE are used:

$$\mathcal{L}_{G|D}(X,Y) = \alpha \cdot MSE(G(X),Y) + \beta \cdot SSIM(G(X),Y) + \gamma \cdot BCE(D(G(X) - D(Y), y). \tag{6}$$

Here $\alpha$, $\beta$, and $\gamma$ denote the weights given to the respective losses. MSE loss was used to ensure the general fidelity of the generated image. However, the loss given to the MSE cannot be too high in comparison to the SSIM and BCE because the differences between HQ ground truth and LQ images in terms of MSE are initially small. SSIM loss on the other hand ensures that the visual perception of the generated image is enhanced, whereas the BCE encourages the generator to produce images similar to the HQ ground truth ones. Altogether, the combined weights of MSE and SSIM accounted for approximately 10% of the total loss.

To compare the ability of our network to produce HQ images, we also performed deconvolution of LQ images. The deconvolution workflow was done using Fiji ImageJ software. For that purpose, we used BatchDeconvolution, PSF generator, and the DeconvolutionLab2 plugins [34–37]. PSF was generated according to the Born-Wolf model [34], with the parameters set to be identical to those used during the experiments, i.e., NA = 1.4, immersion refractive index = 1.515, pixel size = 159 nm and the wavelengths identical to those of the maxima of emission spectra of the fluorophores (461nm, 520nm, and 565nm, for Hoechst 3342, Alexa Fluor 488, and Alexa Fluor 555, respectively). The deconvolution was performed separately for all the channels and was done using the Richardson-Lucy algorithm with 10 iterations [38,39].
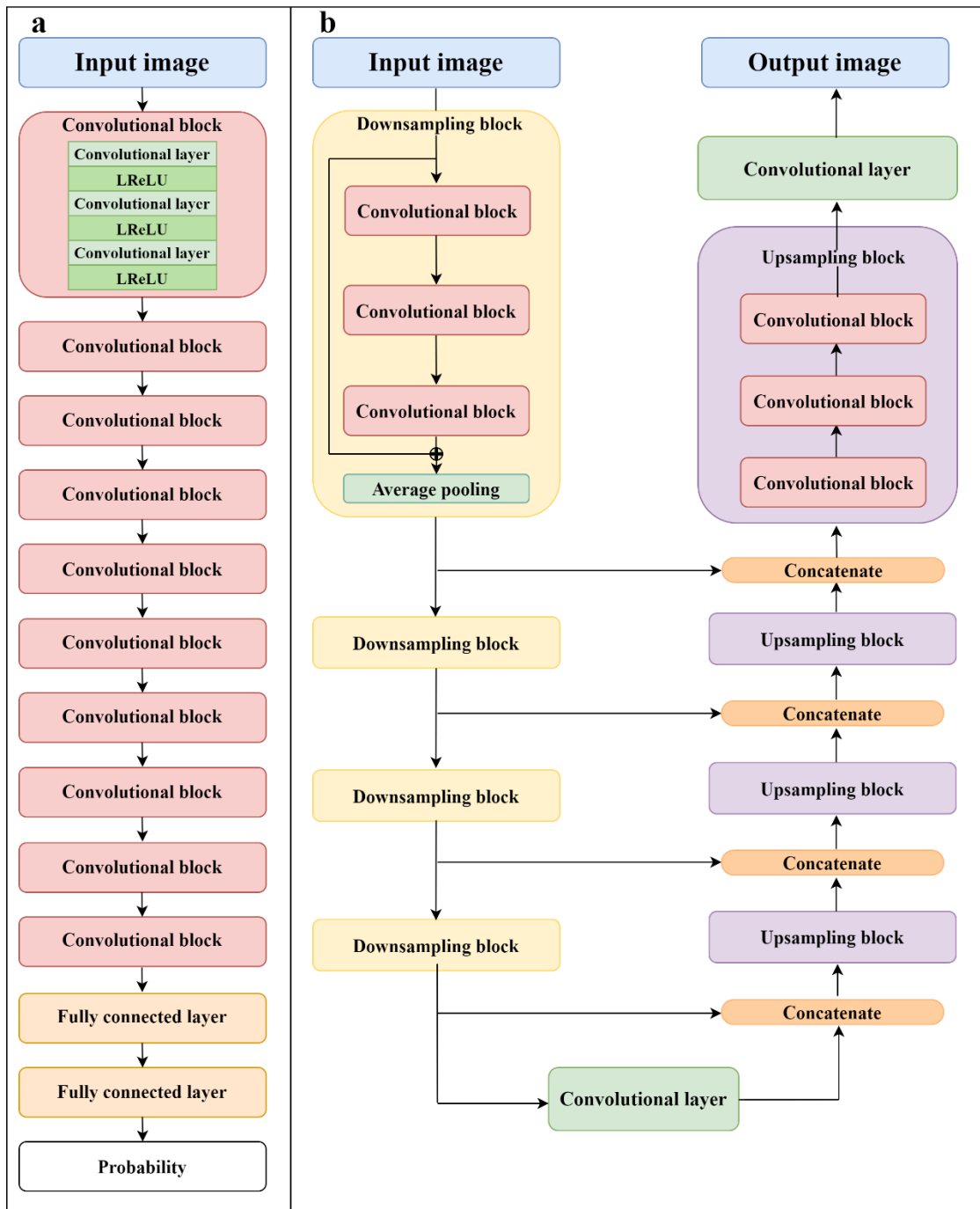
**Figure 1.** The models used in this research. (**a**) The discriminator model (input image can be an HQ ground truth image or an HQ generated image), (**b**) The generator model based on a U-NET architecture (input image is an LQ image, and the output is an HQ generated image).

Altogether training was performed on a set of 480 pairs of images all having the dimensions of 256x256 pixels. The rest of the data was left as a testing and validation sets (120 images). Our GAN architecture is designed to start with random initializations and is optimized using an Adam optimizer with a starting learning rate of $10^{-5}$ for both the discriminator and the generator. It is also worth mentioning that the GAN network continuously switches between training the generator given the discriminator and updating the discriminator by keeping the generator unchanged. In our case, the generator model was saved every 10,000 epochs. Furthermore, during every iteration, the model was validated on the validation image set, and

SSIM and PSNR scores were kept in memory, which allows for saving the best model. This architecture was implemented using Python version 3.8.10, tensorflow version 2.13.0, numpy version 1.23.5, and skimage version 0.19.3. The training was performed using Google CoLaboratory (a cloud-based platform providing access to the graphic processing units). Here, T4 GPU was used and the model was trained for approximately 500,000 iterations. The details of the architecture can be found on the GitHub page. After saving the best model, our solution was validated on unpaired images, which allowed us to assess the model's ability to generalize learned features of the HQ images.

### 3. Results and discussion

In the following sections, we show representative results of the network training, which were obtained on the testing subset of the data. The metrics we used for image comparison are mean squared error (MSE), normalized root mean squared error (NRMSE), structural similarity index (SSIM), and peak signal-to-noise ratio (PSNR). These metrics allowed us to assess the fidelity of the generated images in comparison to the ground truth ones.

To analyze the effectiveness of our network we processed the images of microtubule filaments of mouse embryonic fibroblasts (MEFs) through the GAN model as well as through deconvolution (**Figure 2**). Deconvolution minimized the noise of the LQ wide-field images to some extent (**Figure 2d, h, m**). Nevertheless, our architecture handles this problem in a much more refined way. The microtubular structure is better defined in comparison to the LQ or LQ deconvoluted images. Interestingly, in some cases, our network can reconstruct the intricate microtubular web by removing the excess noise, which indicates the places of the microtubular fibers and allows potentially more precise localization of these structures than in the case of the HQ ground truth image (**Figure 2xi**).

We compared values of MSE, NRMSE, SSIM, and PSNR metrics of representative images of MEF cells taken using confocal microscopy, wide-field fluorescence microscopy, as well as images generated by the network (**Figures 3-5, Table 1**). In both **Figures 3** and **4,** the proposed model was able to restore very intricate details from the cell structures, including actin filaments, microtubules, and even the internal structure of chromatin inside the nuclei. Images in **Figure 3** prove the ability of the network to transfer the high-quality features from the HQ ground truth images to the LQ ones. It can be seen clearly in panels **b** and **c**, as well as **h** and **i**, that the network was able to recover the subtle information about the microtubule structure, which is hard to distinguish in LQ images. Furthermore, in some cases (outlined in **Figure 3**) images generated by the GAN are characterized by a higher level of detailedness when compared to the HQ ground truth images. This is especially visible in panels **f** and **i** of the GAN results where the microtubule structures are more prominent than in the confocal ones. Moreover, evident noise reduction is observable in panel **f** when comparing confocal and generated images. The metrics that we used for comparisons (**Table 1**) indicate that the network was able to learn the ability of an HQ modality to produce HQ images with a high level of fidelity. Nonetheless, the model sometimes struggled to reconstruct actin stress fibers (**Figure 3a-c**, indicated by the white arrow). However, its denoising ability was able to extract information about the microtubule structure from the LQ images (**Figure 3e** and **h**) making them clearly visible (**Figure 3d-i**).
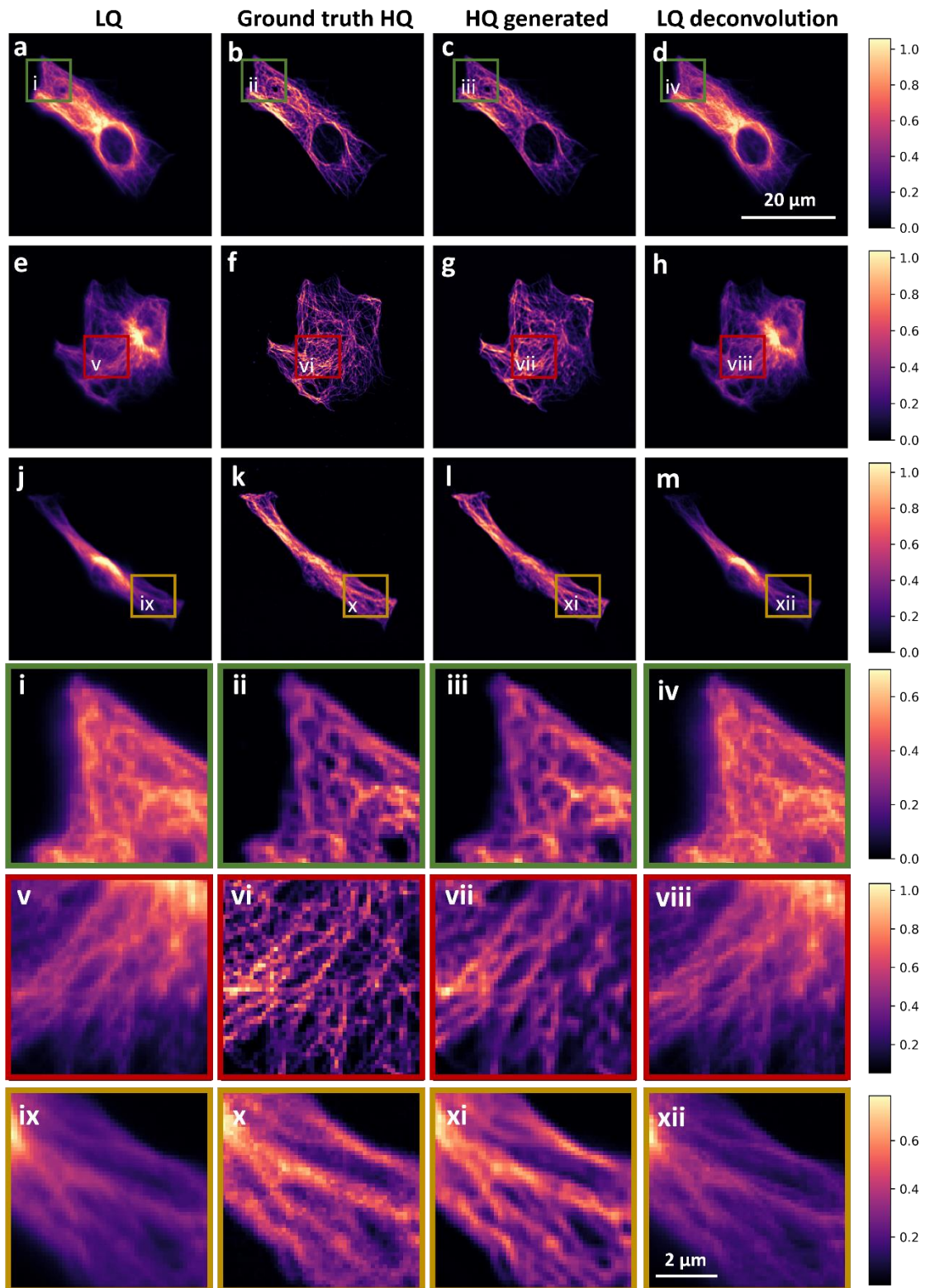
**Figure 2.** The comparison of LQ, ground truth HQ, generated HQ, and deconvolved images of microtubule networks. The color bar on the right corresponds to the normalized fluorescence intensity. Panels (**a – m**) show the LQ input images, ground truth HQ (confocal) images, generated HQ as well as LQ deconvoluted images. The insets (**i – xii**) correspond to the frames of the respective color in the upper figures.
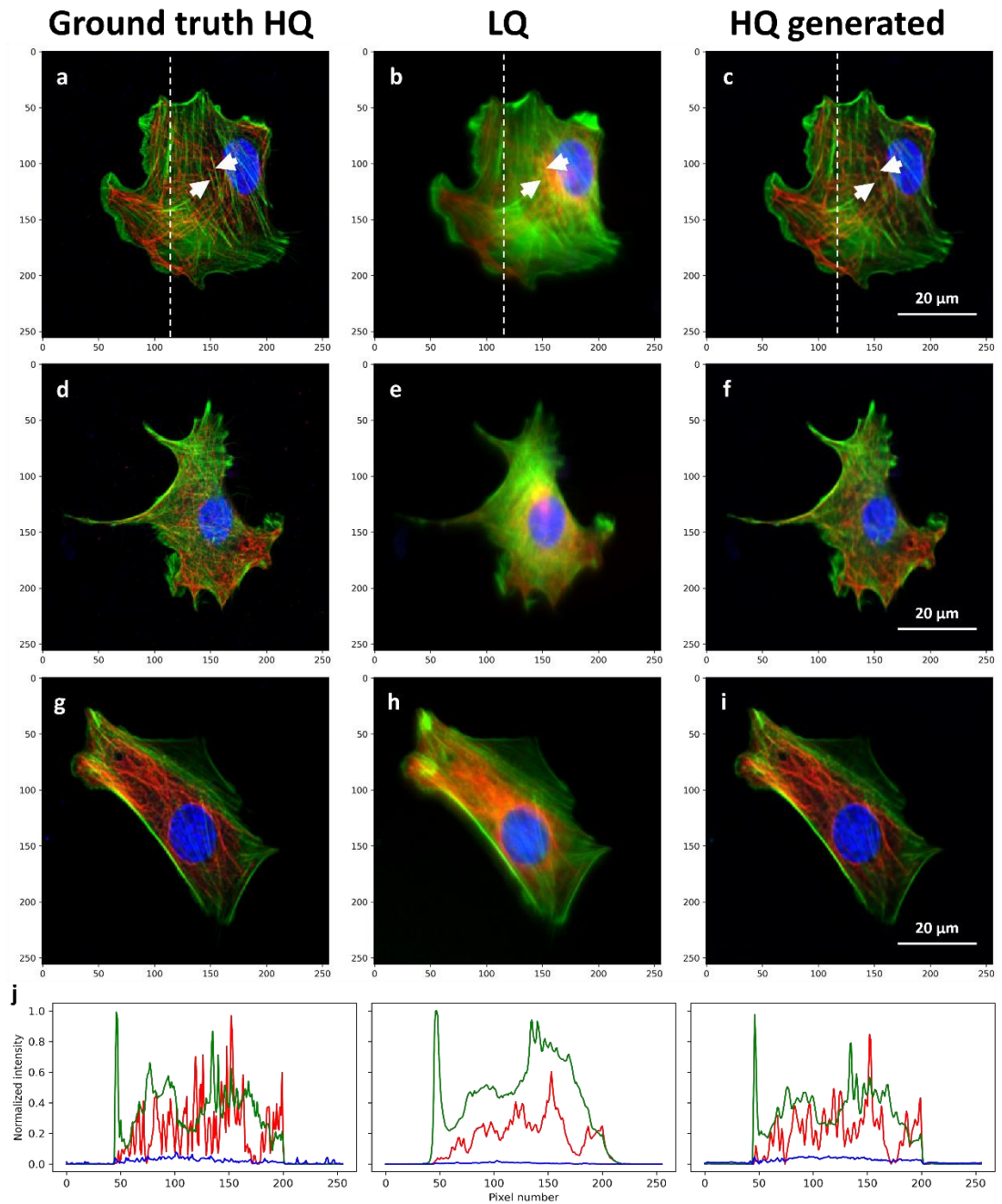
**Figure 3.** Exemplary images showing the network's ability to generate accurate HQ images from the LQ ones. **(a – i)** Comparisons of ground truth HQ (confocal), LQ (WWF), and HQ generated images. The white dashed lines in the **a-c** correspond to the profiles shown in panel **j** (all the profiles are drawn along 128 pixels). Here, red represents microtubule fibers, green - actin filaments, and blue - nucleus. The white arrows point to the regions where the model struggled to reconstruct actin stress fibers. Numbers along the vertical and horizontal axes indicate the pixel number.
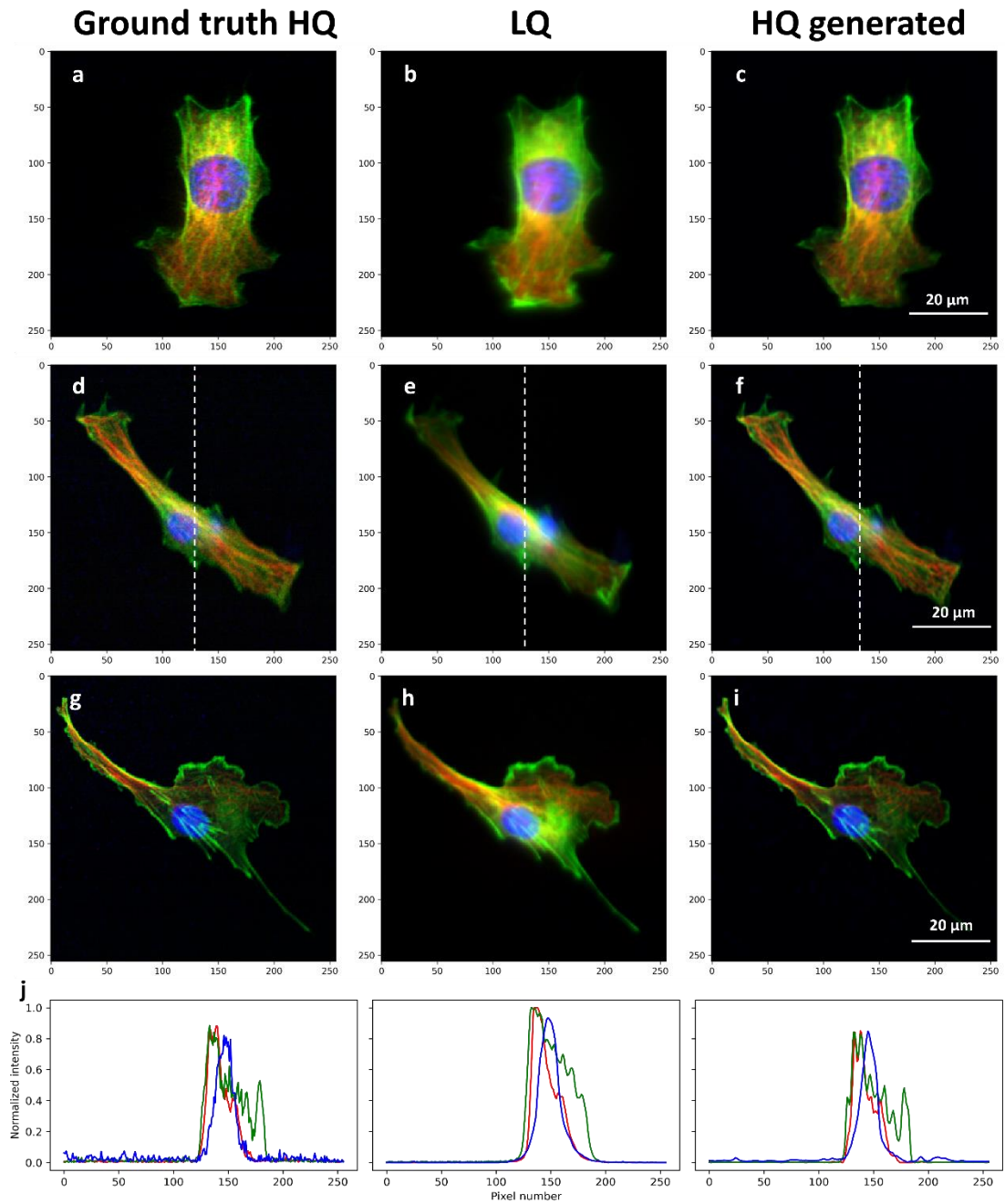
**Figure 4.** Exemplary images showing the network performance in generating HQ images from LQ Images. Panels **(a – i)** show comparisons of ground truth HQ (confocal), LQ (WWF), and HQ-generated images. Interestingly, the network was able to produce images of lower noise than in the HQ ground truth images. The white dashed lines in **d-f** correspond to the profiles shown in the panel **j** (all the profiles drawn along 130 pixels). Here, red represents microtubule fibers, green - actin filaments, and blue - nucleus. Numbers along the vertical and horizontal axes indicate the pixel number.

**Table 1.** Metrics comparing images shown in Figures 2 and 3. Values of the comparisons between ground truth HQ and generated HQ images are bolded. MSE – mean squared error, NRMSE – normalized MSE, SSIM – structural similarity index, PSNR – peak signal-to-noise ratio.

| Comparison | | MSE | NRMSE | SSIM | PSNR |
|---|---|---|---|---|---|
| Fig. 3 | a vs. b | 0.0106 | 0.7249 | 0.8142 | 19.73 |
| | **a vs. c** | **0.0011** | **0.2315** | **0.9283** | **29.65** |
| | b vs. c | 0.0092 | 0.5084 | 0.8292 | 20.35 |
| | d vs. e | 0.0077 | 0.6568 | 0.8320 | 21.15 |
| | **d vs. f** | **0.0010** | **0.2396** | **0.9271** | **29.91** |
| | e vs. f | 0.0070 | 0.5004 | 0.8512 | 21.55 |
| | g vs. h | 0.0066 | 0.6166 | 0.8464 | 21.77 |
| | **g vs. i** | **0.0051** | **0.1708** | **0.9452** | **32.92** |
| | h vs. i | 0.0064 | 0.4582 | 0.8375 | 21.91 |
| Fig. 4 | a vs. b | 0.0037 | 0.3589 | 0.8517 | 24.34 |
| | **a vs. c** | **0.0067** | **0.1437** | **0.9230** | **31.71** |
| | b vs. c | 0.0033 | 0.2852 | 0.8638 | 24.86 |
| | d vs. e | 0.0044 | 0.5002 | 0.6723 | 23.54 |
| | **d vs. f** | **0.0060** | **0.1840** | **0.8410** | **32.23** |
| | e vs. f | 0.0040 | 0.4701 | 0.8281 | 23.97 |
| | g vs. h | 0.0071 | 0.8052 | 0.7570 | 21.46 |
| | **g vs. i** | **0.0005** | **0.2156** | **0.9080** | **32.90** |
| | h vs. i | 0.0068 | 0.5548 | 0.8581 | 21.65 |
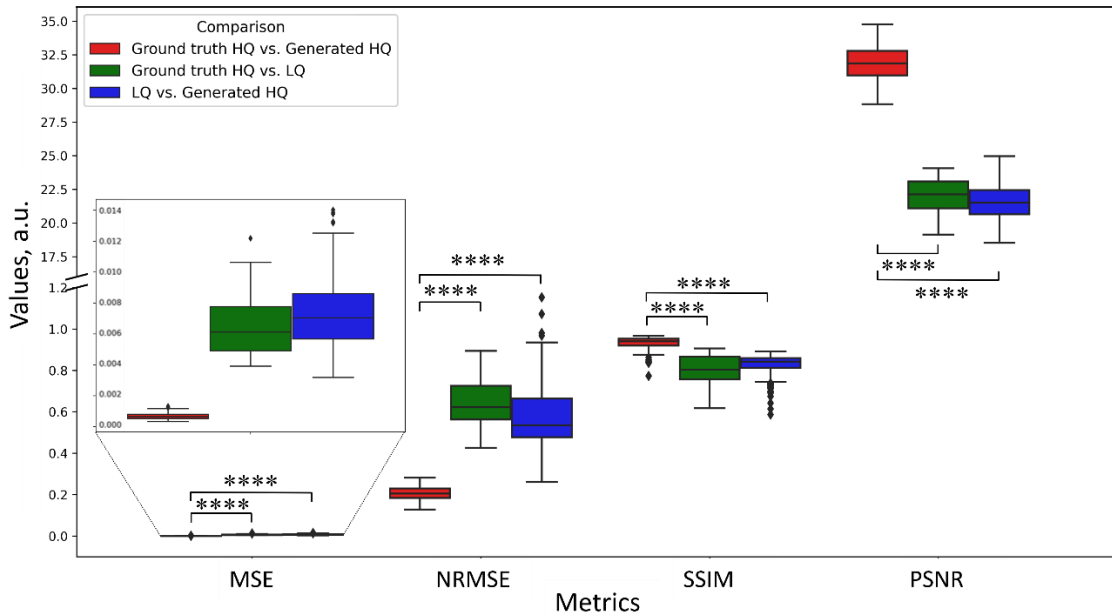


**Figure 5.** Box plots representing differences between the metrics calculated on the testing set. The line within a box represents the median value, the upper and lower box boundaries represent the first and the third quartile respectively, the whiskers represent a range of the data (1.5 times the interquartile range), and the points under or above the whiskers represent the outliers. **** p < 0.0001 (statistics calculated using non-parametric Kruskal-Willis ANOVA test, and *post hoc* Dunn's test).

Additionally, the final model was tested on images, for which ground truth HQ images were not known. The model was able to reconstruct the microtubular structure, which is not clearly seen on the LQ image (**Figure 6**), showing promising robustness to changes in microscopy systems happening over time, such as decreasing light source power or micro-damages of optical elements of the microscope. This procedure also allowed us to estimate to what range experimental conditions and/or microscope settings can influence the outcome of the model.
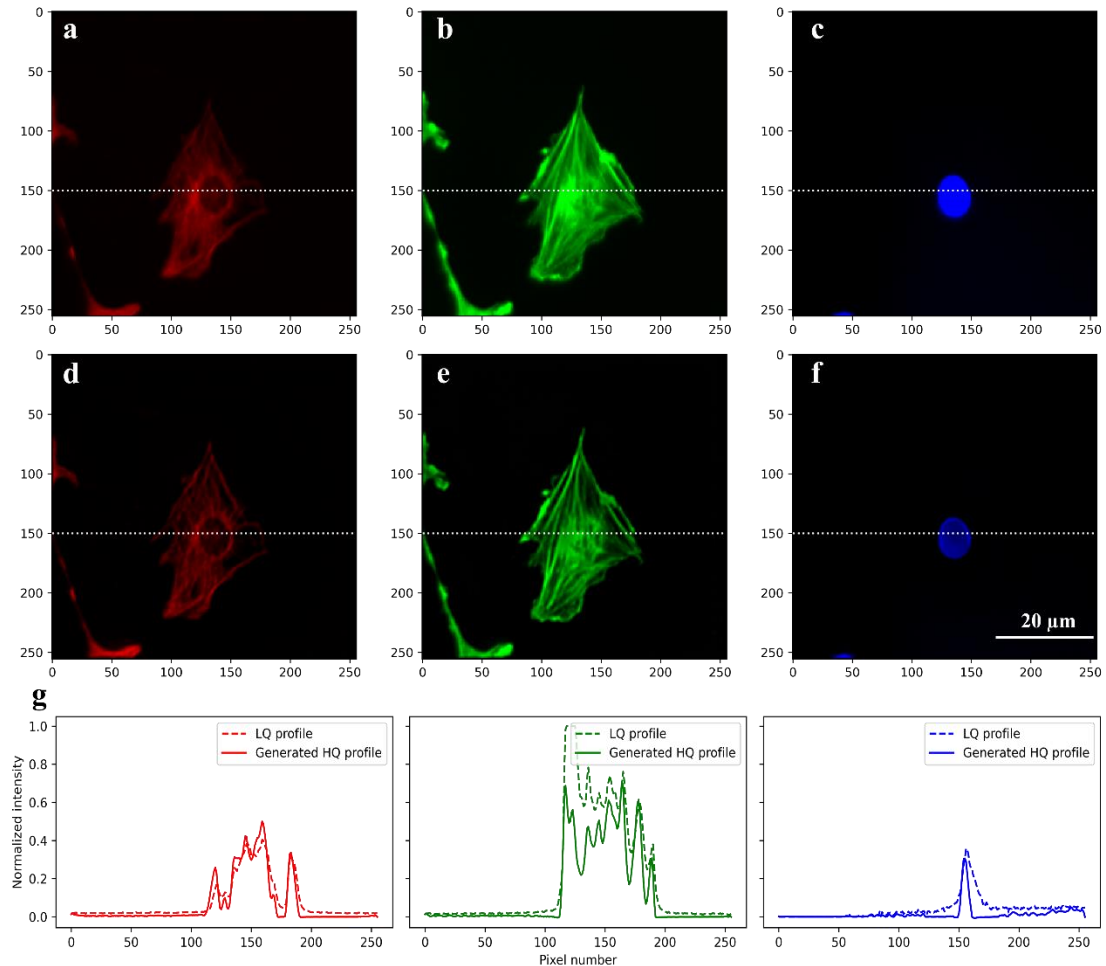


**Figure 6.** Representative results of model performance on an unseen wide-field fluorescence microscopy image. The WFF image was taken under slightly different conditions than the training and testing data. **(a-c)** WFF images, **(d – f)** generated HQ image, **(d)** cross sections through the images (plotted according to the horizontal line in the **(f)** image). Dashed and solid lines represent cross-sections through the WWF and HQ generated images respectively. Red represents microtubule fibers, green - actin filaments, and blue - nucleus. Numbers along the vertical and horizontal axes indicate the pixel number.

## 4. Conclusions

In this paper, we presented a deep-learning algorithm based on a GAN architecture to generate high-quality images based on their low-quality equivalents. To assess the ability of our model to generate HQ images we compared it with a simple process of deconvolution. **Figure 2** shows that our model can reconstruct the intricate cytoskeletal structure based on the LQ images. Furthermore, our model significantly outperforms deconvolution; our model reproduces much more detailed and less noisy images. **Figure 3** shows clearly that the network maps the

resolution from HQ ground truth images to LQ ones with great fidelity, which is also visible in the color-based cross section in **Figure 3j**. The distributions of intensities along the line in images generated by the network and in the HQ ground truth ones are very much alike. Our model manages to generalize the intricate features of HQ imaging very well. In **Figure 4,** our model even outperformed the HQ ground-truth images in terms of quality. **Figure 4a, d,** and **g** show noticeably noisy confocal images, whereas their high-quality generated counterparts do not exhibit similar characteristics. This indicates that the model learned how to generalize HQ features into unseen data. By analyzing the metrics presented in **Table 1** and **Figure 5**, it is evident that in each comparison the ground truth HQ images and generated HQ images are much more alike when compared to LQ and LQ deconvoluted ones. A very convenient metric to measure image similarity is SSIM, which (in contrast to MSE or PSNR) is limited by the upper value of 1. The maximal SSIM value indicates identical images. In **Figure 5** the values of SSIM range from 0.92 to 0.95, which indicates high similarity between images.

In summary, our model can be used for image quality enhancement not only in the case of images collected in the same conditions as the training set but also possibly in the case of images that were obtained in slightly different experimental conditions. However, caution should be taken when interpreting such results. Any modifications, including the efficiency of the microscopy system, staining protocol, the type of cells, etc., may affect the way the model interprets the input LQ data. Nevertheless, the results collected so far present our model as a promising and robust tool for high-resolution image generation.

To our knowledge, this is the first work showing deep-learning-based cross-modality image enhancement between image sets taken on separate imaging systems. Based on the literature [16,40] we believe that this model can be expanded to various other cross-modality setups (like scanning confocal − STED, or TIRF − SIM-TIRF). Thus far there are a couple of initiatives to increase the accessibility of high-quality imaging methods to scientists. For example, *ZeroCostDL4Mic* provides scientists with a database of multiple deep learning-based algorithms to enhance and analyze microscopy images [41]. Furthermore, institutions like Janelia Research Campus or European Molecular Biology Laboratory provide no- or low-cost access to the latest imaging equipment, based on a grant-proposal scheme. Our study opens a gate to a new collaborative approach in imaging, where image enhancement will be dependent on the preparation of a correlated image database of LQ-HQ images, where two imaging systems can be located in different parts of the world. This approach will allow research groups with limited access to advanced microscopy systems to increase their imaging capability, after correlating their system with a high-quality one. We strongly believe that our work will lay the groundwork for the establishment of a multi-institute microscopy cooperative network. This network would enable the virtual pairing of multiple microscopes, even across different continents, to enhance access to high-quality imaging methods.

**Data availability statement**

The data that support the findings of this study are available from the corresponding author upon reasonable request. The GAN software is available to download from the GitHub repository: github.com/panekdominik/Projects/tree/main/GAN_imge_superresolution.

**Authors contribution**
D.P. wrote the software. C.R., M.Sz., and J.S. prepared a paired image database and additional validation images. D.P. tested the algorithm and prepared figures. Z.B., Z.R., and D.P. designed the study. D.P. prepared the first draft of the manuscript. D.P. and Z.B. wrote the final version of the manuscript. K.M., Z.B., and Z.R. supervised the study. All authors contributed to the discussion and accepted the final version of the manuscript.

**Supplementary materials**
1. Data preprocessing

**References**

1. Dazzi, M., Rowland, E. M., Mohri, Z. & Weinberg, P. D. 3D confocal microscope imaging of macromolecule uptake in the intact brachiocephalic artery. *Atherosclerosis* **310**, (2020).
2. White, S. L., Lam, A. T. & Buck, H. D. 3D Imaging for Cleared Tissues and Thicker Samples on Confocal and Light-Sheet Microscopes. in *Methods in Molecular Biology* vol. 2593 (2023).
3. Swaim, W. D. Overview of confocal microscopy. *Methods Mol Biol* **588**, (2010).
4. Elliott, A. D. Confocal Microscopy: Principles and Modern Practices. *Curr Protoc Cytom* **92**, (2020).
5. Hickey, S. M. *et al.* Fluorescence microscopy—an outline of hardware, biological handling, and fluorophore considerations. *Cells* vol. 11 Preprint at https://doi.org/10.3390/cells11010035 (2022).
6. Adamczyk, O., Baster, Z., Szczypior, M. & Rajfur, Z. Substrate stiffness mediates formation of novel cytoskeletal structures in fibroblasts during cell–microspheres interaction. *Int J Mol Sci* **22**, (2021).
7. Haberkiewicz, O. *et al.* Decreased Expression of the Slc31a1 Gene and Cytoplasmic Relocalization of Membrane CTR1 Protein in Renal Epithelial Cells: A Potent Protective Mechanism against Copper Nephrotoxicity in a Mouse Model of Menkes Disease. *Int J Mol Sci* **23**, (2022).
8. Szafranska, K. *et al.* From fixed-dried to wet-fixed to live - Comparative super-resolution microscopy of liver sinusoidal endothelial cell fenestrations. *Nanophotonics* **11**, (2022).
9. Stemmer, A., Beck, M. & Fiolka, R. Widefield fluorescence microscopy with extended resolution. *Histochemistry and Cell Biology* vol. 130 Preprint at https://doi.org/10.1007/s00418-008-0506-8 (2008).
10. Combs, C. A. & Shroff, H. Fluorescence microscopy: A concise guide to current imaging methods. *Curr Protoc Neurosci* **2017**, (2017).
11. Lan, L. *et al.* Generative Adversarial Networks and Its Applications in Biomedical Informatics. *Frontiers in Public Health* vol. 8 Preprint at https://doi.org/10.3389/fpubh.2020.00164 (2020).
12. Wenzel, M. Generative Adversarial Networks and Other Generative Models. in *Neuromethods* vol. 197 (2023).
13. Chen, R. *et al.* Single-frame deep-learning super-resolution microscopy for intracellular dynamics imaging. *Nat Commun* **14**, (2023).

14. Melanthota, S. K. *et al.* Deep learning-based image processing in optical microscopy. *Biophysical Reviews* vol. 14 Preprint at https://doi.org/10.1007/s12551-022-00949-3 (2022).

15. Yang, T., Luo, Y., Ji, W. & Yang, G. Advancing biological super-resolution microscopy through deep learning: a brief review. *Biophysics Reports* vol. 7 Preprint at https://doi.org/10.52601/bpr.2021.210019 (2021).

16. Wang, H. *et al.* Deep learning enables cross-modality super-resolution in fluorescence microscopy. *Nat Methods* **16**, (2019).

17. Qiao, C. *et al.* Rationalized deep learning super-resolution microscopy for sustained live imaging of rapid subcellular processes. *Nat Biotechnol* **41**, (2023).

18. Zhang, H. *et al.* High-throughput, high-resolution deep learning microscopy based on registration-free generative adversarial network. *Biomed Opt Express* **10**, (2019).

19. Park, M., Lee, M. & Yu, S. HRGAN: A Generative Adversarial Network Producing Higher-Resolution Images than Training Sets. *Sensors* **22**, (2022).

20. Quintana-Quintana, O. J., De León-Cuevas, A., González-Gutiérrez, A., Gorrostieta-Hurtado, E. & Tovar-Arriaga, S. Dual U-Net-Based Conditional Generative Adversarial Network for Blood Vessel Segmentation with Reduced Cerebral MR Training Volumes. *Micromachines (Basel)* **13**, (2022).

21. Alam, M. S. *et al.* Super-resolution enhancement method based on generative adversarial network for integral imaging microscopy. *Sensors* **21**, (2021).

22. Huang, B. *et al.* Enhancing image resolution of confocal fluorescence microscopy with deep learning. *PhotoniX* **4**, (2023).

23. Ronneberger, O., Fischer, P. & Brox, T. U-net: Convolutional networks for biomedical image segmentation. in *Lecture Notes in Computer Science (including subseries Lecture Notes in Artificial Intelligence and Lecture Notes in Bioinformatics)* vol. 9351 (2015).

24. Chen, S., Zhao, S. & Lan, Q. Residual Block Based Nested U-Type Architecture for Multi-Modal Brain Tumor Image Segmentation. *Front Neurosci* **16**, (2022).

25. Long, F. Microscopy cell nuclei segmentation with enhanced U-Net. *BMC Bioinformatics* **21**, (2020).

26. Alom, M. Z., Yakopcic, C., Hasan, M., Taha, T. M. & Asari, V. K. Recurrent residual U-Net for medical image segmentation. *Journal of Medical Imaging* **6**, (2019).

27. Khouy, M., Jabrane, Y., Ameur, M. & Hajjam El Hassani, A. Medical Image Segmentation Using Automatic Optimized U-Net Architecture Based on Genetic Algorithm. *J Pers Med* **13**, (2023).

28. Hirose, I. *et al.* U-Net-Based Segmentation of Microscopic Images of Colorants and Simplification of Labeling in the Learning Process. *J Imaging* **8**, (2022).

29. Shihan, M. H., Novo, S. G., Le Marchand, S. J., Wang, Y. & Duncan, M. K. A simple method for quantitating confocal fluorescent images. *Biochem Biophys Rep* **25**, (2021).

30. Schroeder, A. B. *et al.* The ImageJ ecosystem: Open-source software for image visualization, processing, and analysis. *Protein Science* **30**, (2021).

31. Schindelin, J., Rueden, C. T., Hiner, M. C. & Eliceiri, K. W. The ImageJ ecosystem: An open platform for biomedical image analysis. *Molecular Reproduction and Development* vol. 82 Preprint at https://doi.org/10.1002/mrd.22489 (2015).

32. Schindelin, J. *et al.* Fiji: An open-source platform for biological-image analysis. *Nature Methods* vol. 9 Preprint at https://doi.org/10.1038/nmeth.2019 (2012).

33. Wang, Z., Bovik, A. C., Sheikh, H. R. & Simoncelli, E. P. Image quality assessment: From error visibility to structural similarity. *IEEE Transactions on Image Processing* **13**, (2004).

34. Aguet, F., Van De Ville D. & Unser, M. Model-based 2.5-d deconvolution for extended depth of feld in brightfeld microscopy. *IEEE Trans. Image Process* **17**, 1144–1153 (2008).

35. Born, M. , Wolf, E. & Bhatia, A. B. *Principles of Optics: Electromagnetic Teory of Propagation, Interference and Difraction of Light*. (Cambridge University Press, 1999).

36. Kirshner, H. , Aguet, F. , Sage, D. , & Unser. 3-D PSF fitting for fluorescence microscopy: implementation and localization application. *J Microsc* **249**, 13–25 (2013).

37. Baster, Z. & Rajfur, Z. Batchdeconvolution: A Fiji plugin for increasing deconvolution workflow. *Bio-Algorithms and Med-Systems* **16**, (2020).

38. Richardson, W. H. Bayesian-Based Iterative Method of Image Restoration*. *J Opt Soc Am* **62**, (1972).

39. Lucy, L. B. An iterative technique for the rectification of observed distributions. *Astron J* **79**, (1974).

40. Ounkomol, C., Seshamani, S., Maleckar, M. M., Collman, F. & Johnson, G. R. Label-free prediction of three-dimensional fluorescence images from transmitted-light microscopy. *Nat Methods* **15**, (2018).

41. von Chamier, L. *et al.* Democratising deep learning for microscopy with ZeroCostDL4Mic. *Nat Commun* **12**, (2021).

# Cross-system biological image quality enhancement based on the generative adversarial network as a foundation for establishing a multi-institute microscopy cooperative network

Dominik Panek[a, b], Carina Rząca[a, b], Maksymilian Szczypior[b,c], Joanna Sorysz[d],
Krzysztof Misztal[e]*, Zbigniew Baster[b, †]*, Zenon Rajfur[b]*

[a] Doctoral School of Exact and Natural Sciences, Jagiellonian University, ul. Łojasiewicza 11, 30-348 Kraków, Poland

[b] Department of Molecular and Interfacial Biophysics, Faculty of Physics, Astronomy and Applied Computer Science, Jagiellonian University, ul. Łojasiewicza 11, 30-348 Kraków, Poland.

[c] Undergraduate program in Biophysics, Faculty of Physics, Astronomy and Applied Computer Science, Jagiellonian University, ul. Łojasiewicza 11, 30-348 Kraków, Poland.

[d] Undergraduate program in Biomedical Engineering, Faculty of Electrical Engineering, Automatics, Computer Science and Biomedical Engineering, AGH University of Science and Technology, Al. A. Mickiewicza 30, Building B-1, 30-059 Kraków, Poland.

[d] Division of Computational Mathematics, Faculty of Mathematics and Computer Science, Jagiellonian University, 6 Łojasiewicza St., Kraków, Poland

[†] Current address: Cell and Developmental Biology Center, National Heart Lung and Blood Institute, National Institutes of Health, Bethesda, MD 20824-0105, USA

*Author to whom correspondence should be addressed: krzysztof.misztal@uj.edu.pl, zbigniew.baster@nih.gov, zenon.rajfur@uj.edu.pl.

# Supplementary materials

**Supplementary Note 1 – Paired image database preparation**

1. **Cell culture and staining**
   Mouse embryonic fibroblasts (MEF NIH/3T3 - ATCC CRL-1658 |) were culture in medium DMEM Low Glucose medium (L0066, Biowest, Nuaillé, France) supplemented with 10% Gibco FBS (10270106, Thermo Fisher Scientific, Waltham, MA, USA), and 100 I.U./mL Penicillin and 100 µg/mL Streptomycin Solution (L0022, Biowest, Nuaillé, France) at 37°C, 5% CO2, and 100% humidity. Cells were passaged every 2-3 days when the confluence of cells reached about 75%. After at least three passages from thawing, 24 hours before fixation, cells were plated on #1.5 round coverslips, 20 mm in diameter in a six-well plate and cultured with 2 ml of fresh media. 20,000 cells were transferred to each slide in a six-well plate.

   Cells were fixed with 4% paraformaldehyde solution in PBS (20 min at 37°C), followed by incubation with 0.5% TRITON X-100 PBS solution (5 min in RT), and finally 0.1 M glycine solution in PBS (10 min, RT, rocking). Then, the samples were rinsed several times with PBS. After rinsing, samples were blocked using a 4% solution of BSA (bovine serum albumin) in PBST (0.05% TWEEN 20 solution in PBS) for 1 hour in RT.

   Immunofluorescence antibody staining was performed to label the microtubules. Cells were stained overnight with anti-α-Tubulin antibody (1:500 in 4% BSA PBS buffer; T9026, Sigma-Aldrich, St. Louis, MO, USA). Then washed 3 times with PBST (5 min, RT), and stained Alexa Fluor 555-labeled goat anti-mouse IgG (H+L) antibody (1:100 in 4% BSA PBS buffer; A21422, Thermo Fisher Scientific, Waltham, MA, USA) for 1 hour in RT. Then, the samples were washed several times with PBS.

   Thereafter, actin and nucleus were stained for 30 min in RT using PBS solution of Alexa Fluor™ 488 Phalloidin (1:200; A12379, Thermo Fisher Scientific, Waltham, MA, USA), and Hoechst 33342 (2 µg/ml; H3570, Thermo Fisher Scientific, Waltham, MA, USA), respectively. Then, the samples were washed several times with PBS. Before imaging samples were mounted on the Correscopy sample holder (Correscopy, Krakow, Poland).

2. **Wide-field fluorescence and confocal images gathering**
   Two microscopes were used for this purpose: a laser scanning confocal (Zeiss LSM 710 set on Zeiss Axio Observer Z1 body, oil-immersion Plan-Apochromat 40x NA 1.4 objective, ZEN black version 8.10.484 software) and wide-field fluorescence microscopes (Zeiss Axio Observer Z1, oil-immersion EC Plan-Neofluar 40x NA 1.30 Ph3, ZEN blue version 2.3 software). Calibrations were carried out for each microscope before each experiment.

   The calibration consisted of using the dedicated Correscopy software (Correscopy, Krakow, Poland). The first step was to locate the dedicated reference point, then once the orientation of the point was correctly set on the holder and the microscope. Once the calibration was recorded, cells were imaged using 40x oil lenses, preserving the pixel size and the z-step on both microscopes. First, images were taken on the wide-field fluorescence microscope, then the sample was transferred to the laser microscope and calibration was performed again. Moreover, to increase the quality of image alignment we added 200 nm red fluorescent polystyrene beads (F8763, Thermo Fisher Scientific, Waltham, MA, USA) at the paraformaldehyde fixation step.

Additionally, we prepared calibration slides with polystyrene TetraSpeck beads of 100 nm in diameter (T7279, Thermo Fisher Scientific, Waltham, MA, USA). This allowed for the correction of optical defects, i.e. chromatic aberrations, which consist of displacement of the same objects due to the length of light emitted.

The images captured with the wide field microscope were taken at a resolution of 2048x2048, while those with the confocal microscope at a resolution of 1114x1114. This adjustment was made to ensure uniform pixel size across both microscopes. Final alignment was performed using the ImageJ software.

3. **Data preprocessing**

Some of the images were slightly misaligned, i.e. were rotated relative to each other and/or shifted in different axes. The steps of the alignment algorithm were as follows:

   a. evaluation of the rotation angle and rotation of one image (rotation relative to each other of the images was performed using the angle measurement tool in Fiji software),
   b. extraction of a cell from the images by cropping the wide field image with a rectangle of the same size as the confocal image,
   c. evaluation of shifts of images in relation to each other (to determine a possible shift vector, first one corresponding slice was selected from both types of data, then an operation was performed to merge them into one stack and superimpose both images on each other using the method of averaging pixel values)
   d. Possible translation of one of the images (Fiji "Translate" tool was used to reduce the deformation that occurs)
   e. Z-axis image matching (for this purpose, the first and last slices in the stack were found so that they corresponded to each other between the different modalities)